Article

Spin state and deep interior structure of Mars from InSight radio tracking

https://doi.org/10.1038/s41586-023-06150-0

Received: 28 November 2022

Accepted: 27 April 2023

Published online: 14 June 2023

Check for updates

Sébastien Le Maistre[1,2]✉, Attilio Rivoldini[1], Alfonso Caldiero[1,2], Marie Yseboodt[1], Rose-Marie Baland[1], Mikael Beuthe[1], Tim Van Hoolst[1,3], Véronique Dehant[1,2], William M. Folkner[4], Dustin Buccino[4], Daniel Kahan[4], Jean-Charles Marty[5], Daniele Antonangeli[6], James Badro[7], Mélanie Drilleau[8], Alex Konopliv[4], Marie-Julie Péters[1], Ana-Catalina Plesa[9], Henri Samuel[7], Nicola Tosi[9], Mark Wieczorek[10], Philippe Lognonné[7], Mark Panning[4], Suzanne Smrekar[4] & W. Bruce Banerdt[4]

Knowledge of the interior structure and atmosphere of Mars is essential to understanding how the planet has formed and evolved. A major obstacle to investigations of planetary interiors, however, is that they are not directly accessible. Most of the geophysical data provide global information that cannot be separated into contributions from the core, the mantle and the crust. The NASA InSight mission changed this situation by providing high-quality seismic and lander radio science data[1,2]. Here we use the InSight's radio science data to determine fundamental properties of the core, mantle and atmosphere of Mars. By precisely measuring the rotation of the planet, we detected a resonance with a normal mode that allowed us to characterize the core and mantle separately. For an entirely solid mantle, we found that the liquid core has a radius of 1,835 ± 55 km and a mean density of 5,955–6,290 kg m^{-3}, and that the increase in density at the core–mantle boundary is 1,690–2,110 kg m^{-3}. Our analysis of InSight's radio tracking data argues against the existence of a solid inner core and reveals the shape of the core, indicating that there are internal mass anomalies deep within the mantle. We also find evidence of a slow acceleration in the Martian rotation rate, which could be the result of a long-term trend either in the internal dynamics of Mars or in its atmosphere and ice caps.

In an attempt to investigate the deep interior of Mars and the dynamics of its atmosphere, we used data from the Rotation and Interior Structure Experiment (RISE) of the Interior Exploration using Seismic Investigations, Geodesy and Heat Transport (InSight) NASA mission. RISE measures the Doppler shift (or range rate) induced by tiny variations in the rotation and orientation of Mars[1,2] on the two-way radio links, enabled by RISE's X-band coherent transponder, between its two medium-gain antennas and the NASA Deep Space Network.

The RISE experiment accurately characterizes the rotation and orientation parameters of Mars and was specifically designed to measure Martian nutations (periodic motions of the spin axis in space[3]) as a means of studying the core. For each forcing frequency ω ($\omega > 0$) expressed in the inertial frame, the nutation can be decomposed into prograde (P') and retrograde (R') circular motions. Their amplitudes are expressed[3–5] as

$$P'(\omega) = T_F(\omega)P(\omega) \text{ and } R'(\omega) = T_F(-\omega)R(\omega), \quad (1)$$

where P and R are the prograde and retrograde nutation amplitudes of a rigid Mars model, respectively, and the transfer function T_F describes the dependence on the interior structure. For an entirely fluid core (Supplementary Information section 3), the nutation amplitudes are resonantly amplified by the free core nutation (FCN), a normal mode related to the misalignment between the core and mantle rotation axes, according to[3,6]

$$T_F(\omega) = 1 + F\frac{\omega}{\omega - \omega_{\mathrm{FCN}}}, \quad (2)$$

where F is the core amplification factor and ω_{FCN} is the FCN frequency. These transfer-function parameters are related to the interior structure of the planet by

$$F = \frac{A_{\mathrm{f}}}{A - A_{\mathrm{f}}}\left(1 - \frac{\gamma}{e}\right) \text{ and } \omega_{\mathrm{FCN}} = -\Omega\frac{A}{A - A_{\mathrm{f}}}(e_{\mathrm{f}} - \beta). \quad (3)$$

Nutation amplitudes therefore depend on the mean equatorial moments of inertia of the fluid core (A_{f}) and mantle ($A - A_{\mathrm{f}}$), the dynamical polar flattenings of the whole planet ($e = (C - A)/A$, where A and C are the mean equatorial and polar moments of inertia of Mars, respectively) and of the core ($e_f = (C_f - A_{\mathrm{f}})/A_{\mathrm{f}}$, where C_{f} is the polar moment of inertia of the core), the deformation of the core induced by the tidal forcing (γ) and the deformation of the core caused by its differential

[1]Royal Observatory of Belgium, Brussels, Belgium. [2]UC Louvain, Louvain-la-Neuve, Belgium. [3]Institute of Astronomy, KU Leuven, Leuven, Belgium. [4]Jet Propulsion Laboratory, California Institute of Technology, Pasadena, USA. [5]Centre National d'Études Spatiales, Toulouse, France. [6]IMPMC, Sorbonne Université, MNHN, CNRS, Paris, France. [7]Université de Paris, Institut de Physique du Globe de Paris, CNRS, Paris, France. [8]Institut Supérieur de l'Aéronautique et de l'Espace SUPAERO, Toulouse, France. [9]DLR Institute of Planetary Research, Berlin, Germany. [10]Laboratoire Lagrange, Université Côte d'Azur, Observatoire de la Côte d'Azur, CNRS, Nice, France. ✉e-mail: sebastien.lemaistre@oma.be

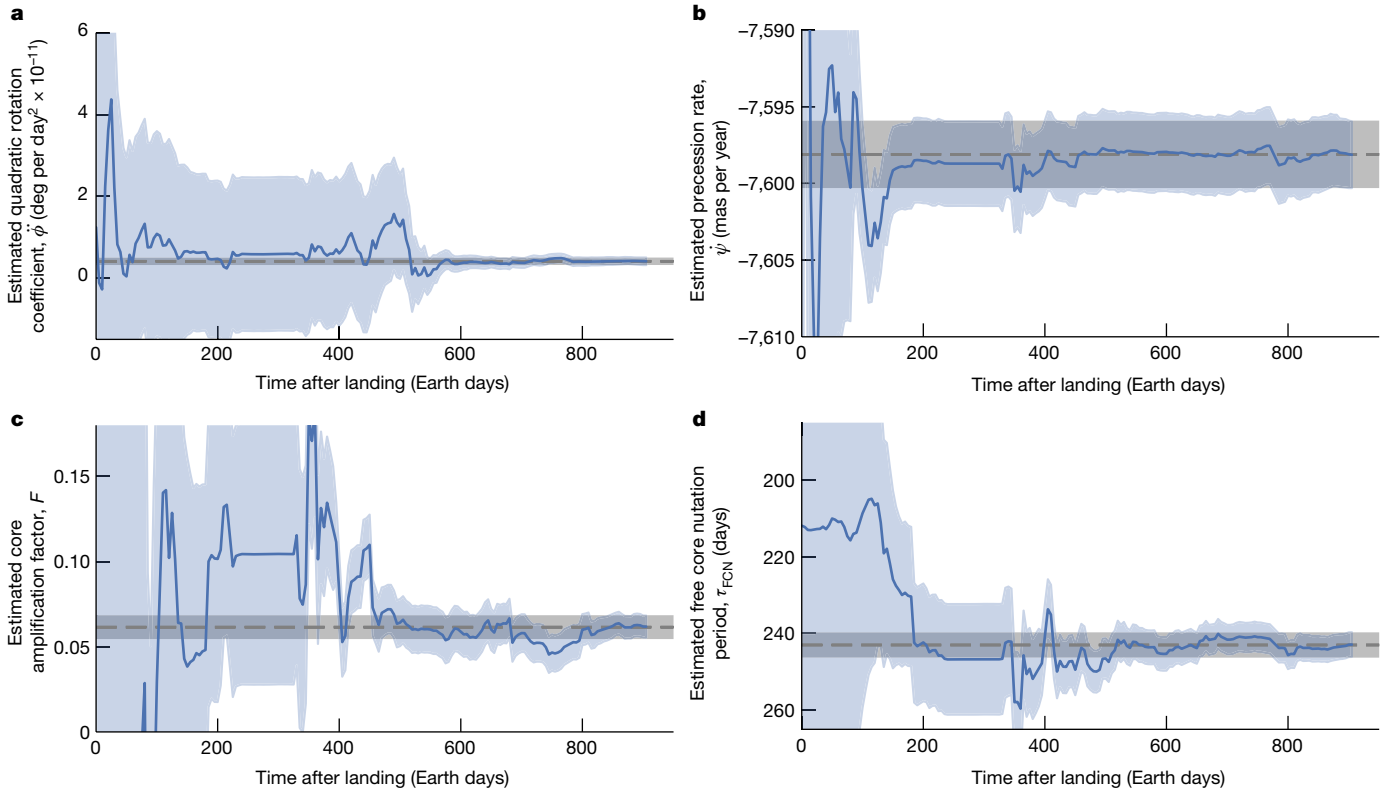

Fig. 1 | Estimates of the main rotation parameters. a–d, Converging solutions of the quadratic rotation coefficient $\ddot{\phi}$ (**a**), precession rate $\dot{\psi}$ (**b**), core amplification factor F (**c**) and FCN period τ_{FCN} (**d**) as a function of time after InSight landing. Dashed lines are our preferred solutions (Extended Data Table 2). Blue shaded regions are formal uncertainties (1σ).

rotation with respect to the mantle (β). Ω is the mean rotation rate of the planet. Nutation analysis based on radiometric measurements is the only technique that can provide direct estimates of these properties of the Martian core. Nutations can also be affected by triaxiality, core–mantle boundary coupling and other rotational normal modes[3]. However, all these effects are small for Mars and are therefore excluded here (Supplementary Information section 9).

The Doppler measurements are analysed by using two different orbitography software packages, MONTE[7] and GINS[8,9] (Supplementary Information section 1), using, as a priori, recently published values for the rotation and polar motion parameters[10] and for the rigid nutation parameters[11] (Methods). Priors for the transfer-function parameters are taken in a large range of values (Supplementary Information section 2). To decorrelate the precession rate and the orientation of the spin axis at the epoch of reference, we also consider data from Viking 1 Lander, in addition to 30 months of more-accurate RISE tracking data (Methods).

Martian rotation and orientation estimates

The estimated rotation and orientation parameters converge after 600 days of operations (Fig. 1), and even sooner for the precession rate, on the basis of combined Viking and RISE data (Supplementary Information section 4).

Separate analyses of Viking and RISE data led to incompatible estimates of the rotation parameters. We therefore estimated separate sets of seasonal spin series for each mission, along with a quadratic term ($\ddot{\phi}$) modelling a spin acceleration. Our estimate of $\ddot{\phi} = 4.11 \times 10^{-12} \pm 9.1 \times 10^{-13}$ degrees per day^2 (Fig. 1a), the first secular (extremely slow) trend detected in the Martian rotation rate, translates into a decrease in Martian day length of 7.6×10^{-4} ms per year, which corresponds to a rotational acceleration of 4.0 ± 0.9 mas yr^{-2}. This is three orders of magnitude larger than that resulting from Phobos tides and than the expected deceleration by the Sun. This rotational acceleration could be the expression of a long-term trend in the internal dynamics of Mars, or in its atmosphere and ice caps. A secular variation of the second-degree gravity zonal coefficient $J_2 = -4.4 \times 10^{-12}$ over one Martian year (an order of magnitude smaller than for Earth) would be consistent with the observed acceleration and could be related to postglacial rebound. It could also result from an extremely slow accumulation of ice at the polar caps (<4 cm per Earth year above the 80° N latitude of the permanent cap), leading to a decrease in atmospheric pressure of less than 0.1 Pa per Martian year, which is below the 1.5 Pa absolute error of the InSight APSS pressure sensor[12].

We detected the small motion (≤40 cm) of a lander in inertial space, owing to the effect on nutations of the Martian liquid core, and obtained estimates for the nutation parameters $F = 0.0615 \pm 0.007$ and $\tau_{FCN} = 2\pi/\omega_{FCN} = -243 \pm 3.3$ days (Fig. 1c,d). Our estimated precession rate, $\dot{\psi} = -7{,}598.1 \pm 2.2$ mas yr^{-1} (Fig. 1b), corresponds to a normalized polar moment of inertia of 0.36419 ± 0.00011 (Supplementary Information section 5). New constraints on the core of Mars can be derived from these values by using a set of models of the interior structure.

Constraints on the interior structure of Mars

We consider two temperature profiles (hot and cold), which are representative end-members of a set of profiles inferred from InSight seismic data (Methods). For the mantle composition, we use the EH45 model[13] and the model from ref. 14 (here denoted YMD), which are based on analyses of Martian meteorites. They represent upper and lower limits for the iron oxide (FeO) content of published mantle compositions[15], and this relates directly to the density of the mantle. Our models of the structure agree with the crustal structure inferred from seismic data (Supplementary Information section 8). Mantle anelasticity, which affects the complex compliances β and γ, is parameterized with a

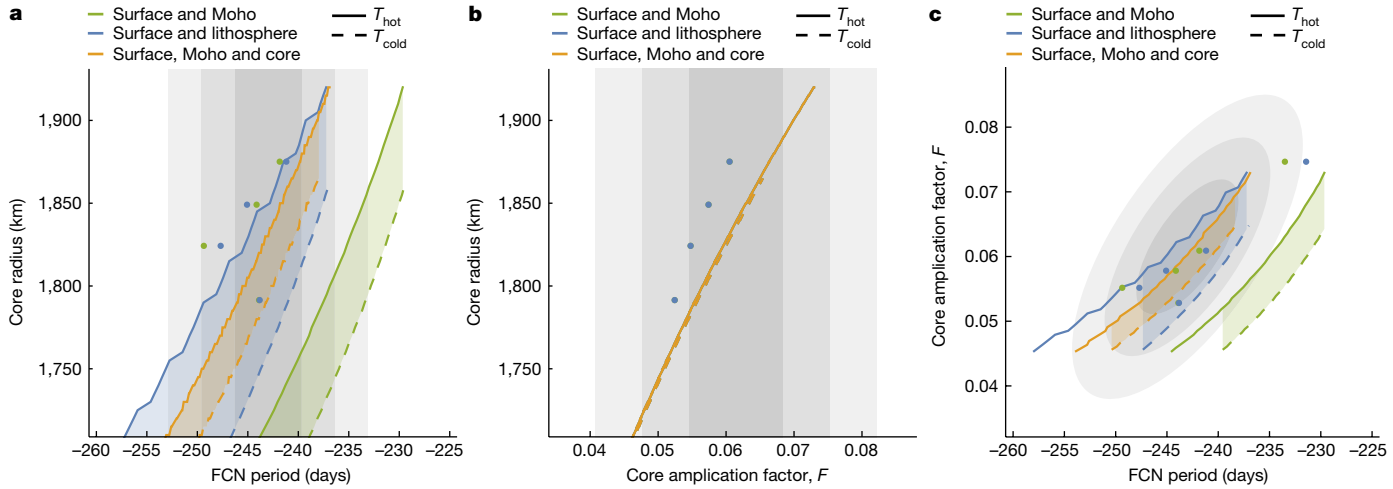

Fig. 2 | Interpretation of nutation parameters in terms of interior structure. **a**–**c**, Core radius versus τ_{FCN} (**a**), core radius versus F (**b**) and correlation between τ_{FCN} and F (**c**) for models based on the YMD mantle composition[14] (coloured areas) and models with a stable magma layer at the bottom of the mantle (circles). Colours differentiate models with one internal load at the Moho (green), one internal load at the bottom of the lithosphere (blue) or two internal loads, located at the Moho and at the bottom of the mantle (orange). In **b**, blue and green lines are hidden behind the orange lines. All models include a surface load associated with the shape of Mars. Solid and dashed lines represent the hot and cold end-member mantle-temperature models, respectively. Grey shaded areas represent 1σ, 2σ and 3σ uncertainties.

frequency-dependent model for shear dissipation (Supplementary Information section 9). Given that τ_{FCN} (the free core nutation period) and F (the core amplification factor) have a relatively small dependence on the composition and thermal state of the liquid core, they are calculated under the assumption that the core is a convecting, liquid alloy of iron and sulfur (Supplementary Information section 12).

Because the estimated core factor F differs from zero at more than 8σ, the core beneath the solid mantle must be liquid. This independently confirms previous inferences from tidal measurements[16] and seismic observations[17]. From F we determine that $A_f = (0.0286 \pm 0.0033) m_a r_a^2$ (Supplementary Information section 13). F (Fig. 2b) is nearly independent of the flattening, the mantle temperature and the composition of the core, and is therefore well suited to determine the radius, R_c, of the fluid core. We find that $R_c = 1{,}835 \pm 55$ km, which is in good agreement with previous results based on geodesy data[18,19] and reflected seismic waves from the core–mantle boundary[17]. The radius of the fluid metallic core might be more than 200 km smaller, however, if the lowest part of the mantle is molten and rotates independently of the solid mantle above (Supplementary Information section 11).

Interpreting the FCN period in terms of interior structure requires us to identify plausible processes that can explain the flattening of the core (equation 3). The simplest model matching both core and surface flattening consists of assuming two mass-sheet anomalies, one associated with the surface topography and the other based deeper in the lithosphere[20]. The latter could result from relief along the crust–mantle interface (the Moho) and from horizontal density variations arising from temperature variations. Additional effects on the core flattening can be caused by density anomalies in the convecting mantle[21,22] and stable boundary layers (thermal or chemical) at the bottom of the mantle[23]. We construct models with two or three mass anomalies that act as static loads: at the surface, at the Moho or at the bottom of the lithosphere, and possibly also at the bottom of the mantle. The depth of the second load notably affects the shape of the core (Supplementary Information section 10).

Models that consider only a second load placed at the Moho require a core radius of less than 1,760 km, which is outside the range inferred from F at 1σ (Fig. 2a,c). Models with a load placed at the bottom of the lithosphere require a relatively thick lithosphere (600 km) to agree with both τ_{FCN} and F, and therefore require a crust highly enriched in heat-producing elements compared with the mantle (Supplementary Information section 7). Temperature profiles directly inferred from seismic data[17] show that the lithosphere can be up to 200 km thinner (Supplementary Information section 7), and many models based on these profiles are not compatible with RISE data unless there is a third load at the bottom of the mantle (analogous to the large low-shear-velocity provinces on Earth[24]) (Fig. 2a,c). Models with a thinner lithosphere can also be reconciled with τ_{FCN} if a fluid dense basal layer is present at the bottom of the mantle (Supplementary Information section 11).

The FCN period indicates a density jump of 1,690–2,110 kg m^{-3} at the core–mantle boundary (Fig. 3). The size of the core radius implies a mean density of 5,955–6,290 kg m^{-3} (Supplementary Fig. 8), which

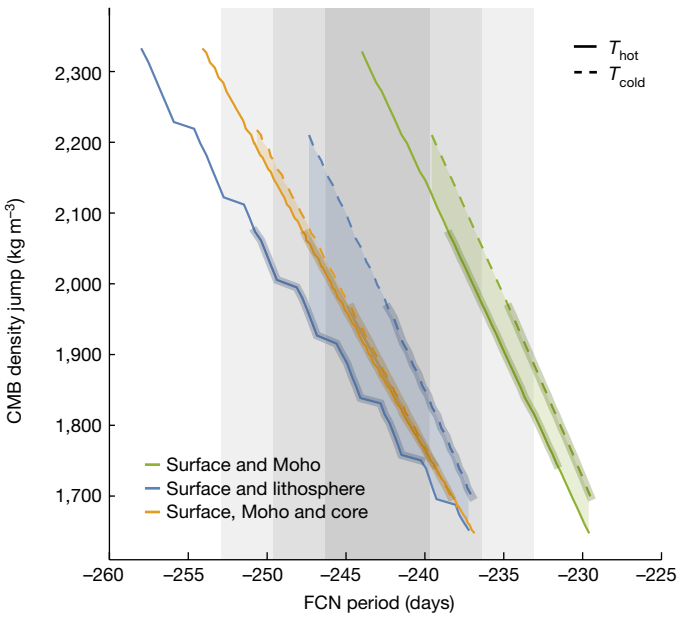

Fig. 3 | Density jump at the core–mantle boundary as a function of FCN period. Models that agree with F (1σ) are represented by thick lines. Colours and dashed lines are as Fig. 2. CMB, core–mantle boundary. The model of the mantle composition is YMD[14].

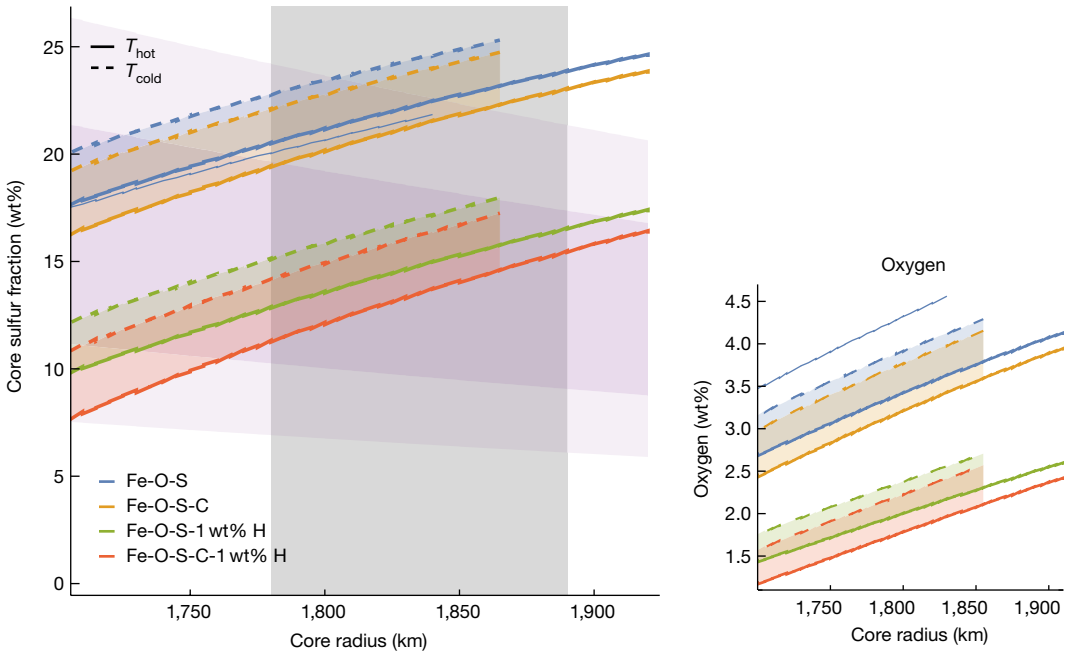

Fig. 4 | Fraction of light elements in the core of Mars. Sulfur concentration in the core as a function of core radius for the YMD mantle model[14] (thick lines) and for the EH45 model[13] (thin line; only Fe–O–S with T_{hot}), and for different core compositions. Dashed curves show models based on a cold mantle temperature; solid lines are for a hot temperature. The grey area represents the core radius inferred in this study (1σ). The darker purple area is the sulfur content (dependent on the core mass fraction) predicted from cosmochemical considerations[24], and the lighter purple area is based on the assumption that the sulfur content of Mars is equivalent to that of chondrites (1.6–5.6 wt%)[32]. The smaller graph to the right shows the wt% of oxygen associated with each model. YMD models based on T_{cold} (ref. 14) match the moment of inertia only if the core radius is less than 1,865 km, and EH45 models based on T_{hot} models match the moment of inertia only if the core is less than 1,840 km (Supplementary Information section 8).

is in the upper range of values proposed previously[17] and requires a substantial amount of light elements alloyed with iron (Fig. 4). The most prominent candidate for a light element is sulfur, which is an abundant and highly siderophile element at core-forming conditions, with a concentration probably below around 20% by weight (wt%), according to cosmochemistry[14,25]. Sulfur alloying to iron during core differentiation comes with a few wt% of oxygen[26], making liquid Fe–O–S the chemically simplest plausible composition. However, if the sulfur concentration in the core lies within the range predicted by cosmochemistry, a core of Fe–O–S is possible only if its radius is at the lower end of our estimate and its temperature is high (Fig. 4). Larger core radii require the presence of additional light elements, such as hydrogen and carbon[14,25,27,28], or a sulfur content equivalent to that of high-iron enstatite chondrites. Given the low solubility of carbon in liquid Fe–S (ref. 29), the composition of the core most compatible with RISE consists of 2.5 ± 0.5 wt% oxygen, 15 ± 2 wt% sulfur and 1.5 ± 0.5 wt% carbon, assuming 1 wt% hydrogen (Fig. 4). A lower amount of light elements is possible if Mars has a fully molten lower-mantle layer[23].

The large amount of light elements, with a sulfur fraction close to the Fe–S eutectic, results in a liquidus temperature substantially below the expected core temperature (Supplementary Information section 12). An inner core is therefore highly unlikely. If an inner core were nevertheless to exist, another rotational mode called the free inner core nutation could affect the 1/2-annual or 1/3-annual prograde nutation[30]. No such signature has been detected in the RISE data (Supplementary Information section 3). The absence of an inner core is also in agreement with the early cessation of an internally generated magnetic field[31].

Online content

Any methods, additional references, Nature Portfolio reporting summaries, source data, extended data, supplementary information, acknowledgements, peer review information; details of author contributions and competing interests; and statements of data and code availability are available at https://doi.org/10.1038/s41586-023-06150-0.

1. Banerdt, W. B. et al. Initial results from the InSight mission on Mars. *Nat. Geosci.* **13**, 183–189 (2020).
2. Folkner, W. M. et al. The rotation and interior structure experiment on the InSight mission to Mars. *Space Sci. Rev.* **214**, 100 (2018).
3. Dehant, V. & Mathews, P. M. *Precession, Nutation and Wobble of the Earth* (Cambridge Univ. Press, 2015).
4. Sasao, T., Okubo, S. & Saito, M. A simple theory on dynamical effects of stratified fluid core upon nutational motion of the Earth. *Proc. IAU Symp.* **78**, 165–183 (1980).
5. Folkner, W. M. et al. Interior structure and seasonal mass redistribution of Mars from radio tracking of Mars Pathfinder. *Science* **278**, 1749–1752 (1997).
6. Yoder, C. F. & Standish, E. M. Martian precession and rotation from Viking lander range data. *J. Geophys. Res.* **102**, 4065–4080 (1997).
7. Evans, S. et al. MONTE: the next generation of mission design and navigation software. *CEAS Space J.* **10**, 79–86 (2018).
8. Marty, J. C. et al. GINS: the CNES/GRGS GNSS scientific software. *3rd Int. Coll. Sci. Fundam. Asp. Galileo Program. ESA Proc. WPP326* **31**, 8–10 (2011).
9. Le Maistre, S. et al. Lander radio science experiment with a direct link between Mars and the Earth. *Planet. Space Sci.* **68**, 105–122 (2012).
10. Konopliv, A. S. et al. Detection of the Chandler wobble of Mars from orbiting spacecraft. *Geophys. Res. Lett.* **47**, e2020GL090568 (2020).
11. Baland, R.-M. et al. The precession and nutations of a rigid Mars. *Celest. Mech. Dyn. Astron.* **132**, 47 (2020).
12. Banfield, D. et al. InSight Auxiliary Payload Sensor Suite (APSS). *Space Sci. Rev.* **215**, 4 (2019).
13. Sanloup, C. et al. Density measurements of liquid Fe–S alloys at high-pressure. *Geophys. Res. Lett.* **27**, 811–814 (1999).
14. Yoshizaki, T. & McDonough, W. F. The composition of Mars. *Geochim. Cosmochim. Acta* **273**, 137–162 (2020).
15. Smrekar, S. E. et al. Pre-mission InSights on the interior of Mars. *Space Sci. Rev.* **215**, 3 (2019).
16. Yoder, C. F., Konopliv, A. S., Yuan, D. N., Standish, E. M. & Folkner, W. M. Fluid core size of Mars from detection of the solar tide. *Science* **300**, 299–303 (2003).
17. Stähler, S. C. et al. Seismic detection of the martian core. *Science* **373**, 443–448 (2021).
18. Rivoldini, A., Van Hoolst, T., Verhoeven, O., Mocquet, A. & Dehant, V Geodesy constraints on the interior structure and composition of Mars. *Icarus* **213**, 451–472 (2011).
19. Khan, A. et al. A geophysical perspective on the bulk composition of Mars. *J. Geophys. Res.* **123**, 575–611 (2018).
20. Wieczorek, M. A., Beuthe, M., Rivoldini, A. & Van Hoolst, T. Hydrostatic interfaces in bodies with nonhydrostatic lithospheres. *J. Geophys. Res. Planets* **124**, 1410–1432 (2019).
21. Kiefer, W. S., Bills, B. G. & Nerem, R. S. An inversion of gravity and topography for mantle and crustal structure on Mars. *J. Geophys. Res. Planets* **101**, 9239–9252 (1996).

22. Defraigne, P., Dehant, V. & Van Hoolst, T. Steady-state convection in Mars' mantle. *Planet. Space Sci.* **49**, 501–509 (2001).
23. Samuel, H. et al. The thermo-chemical evolution of Mars with a strongly stratified mantle. *J. Geophys. Res. Planets* **126**, e2020JE006613 (2021).
24. McNamara, A. K. A review of large low shear velocity provinces and ultra low velocity zones. *Tectonophysics* **760**, 199–220 (2019).
25. Steenstra, E. S. & van Westrenen, W. A synthesis of geochemical constraints on the inventory of light elements in the core of Mars. *Icarus* **315**, 69–78 (2018).
26. Gendre, H., Badro, J., Wehr, N. & Borensztajn, S. Martian core composition from experimental high-pressure metal-silicate phase equilibria. *Geochem. Perspect. Lett.* **21**, 42–46 (2022).
27. Shibazaki, Y. et al. Hydrogen partitioning between iron and ringwoodite: implications for water transport into the Martian core. *Earth Planet. Sci. Lett.* **287**, 463–470 (2009).
28. Zharkov, V. N. The internal structure of Mars: a key to understanding the origin of terrestrial planets. *Sol. Syst. Res.* **30**, 456–465 (1996).
29. Tsuno, K., Frost, D. J. & Rubie, D. C. The effects of nickel and sulphur on the core–mantle partitioning of oxygen in Earth and Mars. *Phys. Earth Planet. Inter.* **185**, 1–12 (2011).
30. Defraigne, P., Rivoldini, A., Van Hoolst, T. & Dehant, V. Mars nutation resonance due to free inner core nutation. *J. Geophys. Res. Planets* **108**, 5128 (2003).
31. Mittelholz, A. et al. Timing of the martian dynamo: new constraints for a core field 4.5 and 3.7 Ga ago. *Sci. Adv.* **6**, eaba0513 (2020).
32. Lodders, K. Relative atomic Solar System abundances, mass fractions, and atomic masses of the elements and their isotopes, composition of the solar photosphere, and compositions of the major chondritic meteorite groups. *Space Sci. Rev.* **217**, 44 (2021).

Methods

Radio-tracking data

The RISE data we used cover the period from 27 November 2018 to 31 May 2021, corresponding to 915 Earth days (890 Martian days). Data from Viking 1 Lander are also used, mostly to decorrelate the rates and angles at the J2000 epoch, whereas data from the Mars Pathfinder and Mars Exploration Rovers were not used because they are scattered and few in number compared with the RISE data (Extended Data Table 1).

We analysed 544 RISE tracking passes, corresponding to around 25,000 Doppler observable data points averaged over 60 seconds, with around 16,150 data points for the east antenna and about 8,900 data points for the west antenna. The nominal pass length of 60 min was reduced to 30 min after 600 days because less energy was available on the InSight lander. The number of passes each week also decreased from 5–7 to 1–3 for the same reason. The antennas are mounted on top of the main deck with fixed pointing directions of east and west. The Earth azimuthal range covered is 77°–130° for the east and 246°–299° for the west antenna. The elevation of Earth at the lander is between 10° and 49°.

In addition to being affected by noise from the RISE instrumentation and the NASA Deep Space Network (DSN) station, the quality of RISE data also depends on the Sun–Earth–probe (SEP) angle, the line-of-sight geometry (especially the line-of-sight elevation above the antennas) and the diameter of the DSN antenna dish. The measurement accuracy, characterized by the standard deviation of the Doppler post-fit residuals, is four times better for RISE (around 1.1 mHz noise for data integrated over 60 s) than for Viking (around 4.5 mHz over 60 s) (Extended Data Fig. 1a,b). The larger spread of the Viking residuals is mainly due to the medium contamination on the Viking S-band data.

Preprocessing of measurements

The refraction of RISE radio waves travelling through the troposphere and ionosphere of Earth and, to a lesser extent, the Martian troposphere imparts a phase delay on the signal. The contribution of the atmosphere of Earth is modelled using information provided by the DSN RadioMetric Data Conditioning Subsystem in the form of TRK-2-23 files. These files include both seasonal and daily (second-order) calibrations, expressed as polynomials modelling the tropospheric and ionospheric delay of Earth at the zenith. The delay from the troposphere ($\Delta\rho$) is modelled as:

$$\Delta\rho = M_{\mathrm{dry}}(d_{\mathrm{o}} + d_{\mathrm{b}} + d_{\mathrm{p}}) + M_{\mathrm{wet}}(w_{\mathrm{o}} + w_{\mathrm{b}} + w_{\mathrm{p}}),$$

where d_{o} is the zenith dry offset, d_{b} is the zenith dry bias parameter and d_{p} is a polynomial model of the zenith dry delay. Similarly, w_{o} is the zenith wet offset, w_{b} is the zenith wet bias parameter, and w_{p} is a polynomial model of the zenith wet delay. Of these, d_{o}, d_{p}, w_{o} and w_{p} are models provided by the DSN media calibration system and given in the RISE archives (https://pds-geosciences.wustl.edu/insight/urn-nasa-pds-insight_rise_raw/data_tro/). M_{dry} and M_{wet} are the dry and wet Niell mapping functions[33], respectively, which were used to obtain the delay at specific elevations. The dry troposphere accounts for about 90% of the total media delay. The associated uncertainties are much smaller than for the wet part because these short-term variations are difficult to calibrate using data from the Global Navigation Satellite System. This is why d_{b} is set to zero and w_{b} is estimated on a per-pass basis (details below). Daily calibrations for the ionosphere delay are an order of magnitude lower than those for the seasonal troposphere (Extended Data Fig. 2a). Calibrations for the Martian troposphere delay, performed following a previously published method[34], is indispensable for a reliable retrieval of the FCN parameters. At low elevations its contribution is close to that of the daily Earth troposphere corrections (Extended Data Fig. 2a). The main source of inaccuracy in the contribution of the Martian troposphere predicted by the model results from the mapping function used. We tested both the 'flat' and the 'geometric' mapping functions presented previously[34], which led us to conclude that the mapping function actually has little influence on the estimation of nutation parameters from RISE data.

Following a previous procedure[35], the raw TRK-2-34 tracking data, sampled at 0.1 s by the DSN Block V Closed Loop Receiver, are compressed to 60 s and then filtered on the basis of the SEP angle (or elongation) and the identification of outliers. Around 2,100 data points collected at SEP < 15° (blue squares in Extended Data Fig. 2b) are discarded because they are strongly affected by solar plasma noise. A wet troposphere bias parameter, w_{b}, is estimated for each pass with an a priori uncertainty of 4 cm (Extended Data Fig. 2c). The 1σ variation among each pass was approximately 5 cm. We removed 86 passes larger than 1σ, reducing the number of data points used from around 25,000 to 20,500. We filtered out 2,700 additional measurements with Doppler residuals larger than 3σ of the residuals (that is, 3 × 1.1 mHz for RISE and 3 × 4.5 mHz for Viking 1 Lander), leading to around 17,000 points (or about 285 h) of RISE tracking used in our solutions and around 11,000 points (or about 185 h) of Viking tracking. Removing outliers on a per-pass basis instead leads to around 1,000 extra points for RISE and about 500 extra for Viking. This approach yields consistent estimates of Martian rotation and orientation parameters compared with the nominal settings, as long as these points are adequately de-weighted on the basis of the noise of the pass. Removal and weighting of the data on a per-mission, rather than a per-pass, basis was preferred because of the more-conservative estimate uncertainties it provides.

Data analysis

The 60-s Doppler measurements were analysed using the Jet Propulsion Laboratory (JPL) Mission analysis Operations and Navigation Toolkit Environment (MONTE) program[7] and the Centre National d'Etudes Spatiales (CNES) Géodésie par Intégrations Numériques Simultanées (GINS) software[8,9,36]. Both software packages are designed for orbital determination and trajectory optimization and analysis using an iterative least-squares procedure.

The trajectories of Earth and Mars are obtained from the DE431 planetary ephemerides[37] but preliminary computations performed with DE440 led to estimates of Martian rotation and orientation parameters compatible with our nominal solution at 1σ. Phobos and Deimos states are taken from the mar097 JPL ephemeris[38]. DSN antenna positions are taken from global VLBI solutions. A model of rigid and ocean loading is introduced, and Earth plate tectonics are modelled with constant drifts based on GNSS, VLBI, SLR and DORIS observations. The orientation parameters of Earth are provided by JPL's Time and Earth Motion Precision Observation group for MONTE and the International Earth Rotation and Reference Systems Service (IERS) for GINS. Tidal deformations of the surface of Mars are accounted for using the conventional solid Earth tidal model[39,40] (IERS conventions). This generates variations in the 3D position of the lander of only a few millimetres in amplitude (10–100 times smaller than displacement from the liquid core). Deformations resulting from Martian atmospheric loading have been excluded.

Rotation models for celestial bodies are implemented differently in the two software packages. GINS uses rotational elements with respect to the International Celestial Reference Frame (ICRF); that is, the right ascension, α, and the declination, δ, angles to position the pole of Mars with respect to the Earth equator of epoch (J2000), and the rotation angle W to locate the prime meridian[41] (Extended Data Fig. 3a). Five elementary rotations are needed to transform the lander position vector r_{icrf}, expressed in the coordinates of the ICRF, into the coordinates of a Mars body-fixed reference frame, r_{bf}:

$$r_{\mathrm{bf}} = R_y(-X_p)R_x(-Y_p)R_z(W)R_x\left(\frac{\pi}{2} - \delta\right)R_z\left(\frac{\pi}{2} + \alpha\right)r_{\mathrm{icrf}}. \quad (4)$$

MONTE uses Euler angles to describe the rotation of Mars, following a previous formulation[42] (Extended Data Fig. 3a):

- $I = I_0 + \dot{I}(t - t_0) + \Delta I$ is the inclination (obliquity) of the true equator of Mars with respect to the Martian mean orbital plane at epoch;
- the longitude $\psi = \psi_0 + \dot{\psi}(t - t_0) + \Delta\psi$ locates node C between those two planes and is measured from node A.
- The spin angle $\phi = \phi_0 + \dot{\phi}(t - t_0) + \Delta\phi - \Delta\psi \cos I_0$ gives the position of the prime meridian of Mars and is measured along the true equator of date starting from node C.

The Δ quantities are series of variations at harmonics of the orbital period of Mars (such series also exist for the α, δ and W angles). The transformation between r_{icrf} and r_{bf} is performed using seven elementary rotations:

$$r_{\mathrm{bf}} = R_y(-X_p)R_x(-Y_p)R_z(\phi)R_x(I)R_z(\psi)R_x(J)R_z(N)r_{\mathrm{icrf}}. \quad (5)$$

The longitude N and inclination J orient the Martian mean orbit of epoch with respect to the ICRF. (X_p, Y_p) are the components of polar motion taken[10] in our a priori model. They are not estimated because of a lack of sensitivity of the low-latitude InSight mission to such small signals[9]. Adding future radio science data from higher latitudes would help to disentangle these parameters from the rest of the parameter set[43].

We compute pre-fit Doppler residuals to visualize the quality of our a priori model and the potential of the new data to improve the model. None of the previous a priori models[10,44] flatten the residuals (Extended Data Fig. 1c), revealing their limitation if we assume that the errors in the non-rotation parameters are much smaller than the errors in the rotation parameters, as we think is the case. Note that the last published estimate[44] for the rotation rate (350.8919825° per day) is actually $\dot{W}$ rather than $\dot{\phi}$ as claimed by the authors. The corresponding value for $\dot{\phi}$ is 350.891985377° per day.

Full-arc 30-months dataset solution

Instead of determining the amplitudes of nutation (P', R' in equation (1)), we estimated the F and $\tau_{\mathrm{FCN}} = 2\pi/\omega_{\mathrm{FCN}}$ parameters of the nutation transfer function T_F (equation (2) and Supplementary Information section 4). The estimates of τ_{FCN}, F and $\dot{\psi}$ are not stable over time (Extended Data Fig. 4) with the classic rotation model[42], so we extended the model and refer to it as the post-dust-storm model.

With respect to the classic model, the new one has extra quadratic terms in the parametrization of the longitude and obliquity angles, as predicted by the precession–nutation theory[11]. We also add terms at periods related to the motion of Phobos and Deimos for the obliquity and longitude angles. We keep the spin periodic series $\Delta\phi$ of the classic model, with terms from the annual to the quarter-annual periods[42,44]:

$$\Delta\phi = \sum_{j=1}^{4} (\phi_{cj}\cos(jM) + \phi_{sj}\sin(jM)), \quad (6)$$

where M is the mean anomaly and the sine amplitudes are corrected for relativistic effects[45]. An extra set of annual amplitudes (ϕ'_{c1}, ϕ'_{s1}) is used to fit the slope observed in the early part of the mission (Extended Data Fig. 1d). This slope in the residuals could be due to the decay of the global dust storm that occurred a few months before the InSight landing. The pressures recorded by InSight were noticeably lower than those of Viking at similar solar longitudes[46] in the first 100–200 days of data, providing evidence of a global dust storm that perturbed the carbon dioxide cycle and resulted in a large deposition of ice at the northern polar cap, which lasted longer than usual after the storm[47]. This accumulation of CO_2 ice at the polar caps temporarily caused the planet's rotation to speed up. Our estimates for those annual amplitudes represent a monotonically decreasing contribution to the spin angle over the first roughly 150 days of the RISE mission, which might actually characterize the temporary post-dust-storm deceleration in the rotation of Mars.

Because separate analyses of Viking and RISE data lead to incompatible estimates of both the rotation rate and the amplitudes of the periodic variations, we estimate in the global inversion separate sets of seasonal spin series for each era, along with a quadratic term ($\ddot{\phi}$) modelling a spin acceleration. The estimated amplitudes for each era are different from previously published solutions[10,44,48] and also from the current standard model[41] of the International Astronomical Union, which is driven by data from Viking. The reason for the difference between the spin-angle variations for the two eras is still under investigation but is probably related to the poor quality of the Viking data.

The final adopted rotation model is given by

$$\begin{aligned} \psi(t) &= \psi_0 + \dot{\psi}(t - t_0) + \ddot{\psi}(t - t_0)^2 + \Delta\psi, \\ I(t) &= I_0 + \dot{I}(t - t_0) + \ddot{I}(t - t_0)^2 + \Delta I, \\ \phi(t) &= \phi_0 + \dot{\phi}(t - t_0) + \ddot{\phi}(t - t_0)^2 + \Delta\phi \\ &\quad -\Delta\psi \cos I_0 + \Delta\phi_{\mathrm{dust}}, \end{aligned} \quad (7)$$

where $\Delta\psi$ and ΔI are the nutation series and $\Delta\phi$ is the spin series defined in equation (6) with amplitudes estimated separately for the Viking and RISE eras. $\Delta\phi_{\mathrm{dust}} = \delta\phi_{c1}\cos(M) + \delta\phi_{s1}\sin(M)$ for the first 150 days of RISE data and 0 elsewhere, with $\delta\phi_{c1} = \phi'_{c1} - \phi_{c1}$ and $\delta\phi_{s1} = \phi'_{s1} - \phi_{s1}$ being the 'dust parameters'. With the post-dust-storm rotation model (equation (7)), our FCN solution is equal to −242.8 ± 3.8 days for MONTE and −243.0 ± 2.7 days for GINS when the full set of selected data is used. The 30-months core amplification factor solutions for both software packages are in good agreement with each other as well (see full-arc solutions in Supplementary Table 1). F is more sensitive to the radius of the core than is τ_{FCN}, which is mostly affected by its shape. The recent seismic data provided by InSight's SEIS experiment constrained the core radius to 1,830 ± 40 km (ref. 17). This corresponds to a core factor ranging between 0.055 and 0.065 (Fig. 2b), which is in good agreement with the RISE solution of $F = 0.0615 \pm 0.007$.

To ensure that the noisy data from Viking do not pollute our estimates, we also calculated a nutation solution using only RISE data. Because it is impossible to decorrelate rates and angles at epoch using only RISE data, we made different runs, fixing the t_0 angles to different values (our estimate here or previous values[10]) and/or fixing the quadratic term to zero ($\ddot{\phi} = 0$) or to our nominal estimate. The estimates of the nutation parameter remain consistent with our nominal solution (within our 1σ envelope), showing that Viking data have a negligible contribution to our nutation solution.

Our estimated precession rate $\dot{\psi} = -7{,}598.1 \pm 2.2$ mas yr^{-1} (Fig. 1b) is less than 3σ smaller than previous estimates obtained from lander data[44] and about 4σ smaller than the last solution from the orbiting spacecraft[10]. The difference with the previous lander solution[44] results from the longer RISE data coverage, from the change in our rotation-rate estimate (now corrected for the observed secular acceleration), and from looser a priori constraints on the values of the angles at the J2000 epoch, ψ_0 and I_0, which are highly correlated with precession ($\dot{\psi}$) and obliquity ($\dot{I}$) rates (see a priori constraints in Supplementary Table 1 and correlation matrix in Extended Data Fig. 3b).

Models of the interior structure

The core amplification factor F and the FCN period depend strongly on the state and shape of the core, on the principal moments of inertia of the core and mantle, and on the ability of the mantle to deform. We construct our models in a two-step process: we first build spherical symmetric models (detailed below) and in the second step they are deformed by the effect of rotation and internal loading (Supplementary Information section 10).

We assume a spherically symmetric, three-layer model of the interior structure made of a crust overlying a solid mantle and a liquid core. For each considered crustal structure, mantle composition and temperature, and core temperature profile, we compute a whole-planet model

as described previously[18]. The free parameters are the core radius and the correlated values of the crustal thickness and density (Supplementary Information section 8). The amount of light elements is set such that the models match the observed mass of Mars, and only models agreeing with the moment of inertia are retained. Because the FCN period depends on the moment of inertia of the core through its density, only combinations of light elements can be constrained.

We use two mantle compositions models that roughly delineate the spread in mantle densities expected from published mantle models: the YMD model[14] and the EH45 model[13]. The FeO content of the YMD model[14] is low in comparison to that of the EH45 model and to other published models[49]. We calculate the equilibrium mineralogy and phase proportions in the mantle, as well as its density and elastic properties, using the Gibbs energy-minimization software Perple_X (ref. 50) based on a previously published thermodynamic formulation and database[51] and considering two end-member temperature profiles (T_{hot} and T_{cold}) deduced from 3D thermal-evolution studies of Mars (Supplementary Information section 7).

The present thermal state of the liquid core depends mainly on the not-well-known heat flow at the core–mantle boundary and on the thermal conductivity of the core material. The core temperature profile is likely to be subadiabatic, between that of an isotherm and the adiabat, in agreement with the absence of a present-day core dynamo[52]. We assume that the fully liquid metallic core is either convecting or isothermal.

A large amount of light elements is required to match the core density[17,18,53], with a sulfur fraction close to the Fe–S eutectic, implying a core liquidus temperature much lower than any plausible estimate of the present-day temperature of the Martian core. As such, the presence of an inner core is highly unlikely, although the presence of remelting iron-rich snow in the core cannot be excluded (but has been excluded in our models). Formation conditions and geochemical models indicate that sulfur is the main light element in the core, together with smaller amounts of oxygen, carbon and hydrogen[14,25,27,28]. We model the core as an Fe–O–S–C–H alloy (Supplementary Information section 6). The abundances of the different light elements are not independent of each other. The correlation between the amount of sulfur and oxygen is described by a multistage core-formation model[26]. The correlation with the other light elements is not well known and has been excluded here. The amount of carbon is set to its saturation limit[54] for the conditions at the core–mantle boundary. The solubility of hydrogen in liquid iron at the conditions of the formation of the Martian core is controversial. It is difficult to constrain the abundance of hydrogen in the Martian core, with published results[27,55–58] ranging between 60 ppm and 1.8 wt%. Instead, we consider the hydrogen content of the core to be a free parameter and determine its amount such that the core density agrees with the findings in our study and also with cosmochemical constraints about the permissible amounts of sulfur in the core.

The equations of state for the liquid core used here (Supplementary Information section 6) are considerably improved with respect to those used previously[17]. The Fe–S system equation of state is based on a much larger set of experimental results, and the inclusion of the non-ideal mixing behaviour of the Fe–FeS and Fe–FeO binaries is taken into account. Neglecting non-ideality in Fe–FeS can result in underestimating the fraction of sulfur in the core by almost 4 wt%, and overestimating the amount of oxygen in Fe–FeO by almost 1 wt%.

The non-elastic behaviour of the mantle and crust is described by a frequency-dependent but depth-independent model of shear dissipation[59]. The parameters of the complex shear modulus are chosen such that the semidiurnal tidal Love number, k_2, the period of the Chandler wobble and the secular acceleration of Phobos agree with observations (see supplementary table 6 of ref. 10).

The compliances required for the calculation of F and the FCN period (see equations (1)–(3) and Supplementary Information section 9) are calculated from spherical models following a previously published method[3].

Data availability

The RISE data that support the findings of this study are available on the Planetary Data system: https://pds-geosciences.wustl.edu/missions/insight/rise.htm. Doppler data for Viking are in the REDUCED directories: https://pds-geosciences.wustl.edu/missions/mpf/radioscience.html. DSN media calibration files are given in the RISE PDS archives: https://pds-geosciences.wustl.edu/insight/urn-nasa-pds-insight_rise_raw/data_tro/. The full correlation matrix is available as source data for Extended Data Fig. 3b. Source data are provided with this paper.

Code availability

Distribution of the MONTE navigation code is restricted by the Export Administration Regulations of the US Department of Commerce. Eligible readers may request a copy of MONTE, under a licence that does not permit redistribution, at https://montepy.jpl.nasa.gov/. GINS software is the property of CNES. It can be used for research only; any other commercial or non-commercial uses are strictly prohibited. CNES grants to the GINS Licensee (natural person) a free non-exclusive licence.

33. Estefan, J. A. & Sovers, O. J. *A Comparative Survey of Current and Proposed Tropospheric Refraction-Delay Models for DSN Radio Metric Data Calibration*. JPL Publication 94-24 (NASA 1994).
34. Le Maistre, S. Martian lander radio science data calibration for Mars troposphere. *Radio Sci.* **55**, e2020RS007155 (2020).
35. Buccino, D., Border, J. S., Folkner, W. M., Kahan, K. & Le Maistre, S. Low-SNR Doppler data processing for the InSight radio science experiment. *Remote Sens.* **14**, 1924 (2022).
36. Le Maistre, S., Rosenblatt, P., Dehant, V., Marty, J.-C. & Yseboodt, M. Mars rotation determination from a moving rover using Doppler tracking data: what could be done? *Planet. Space Sci.* **159**, 17–27 (2018).
37. Folkner, W. M., Williams, J. G., Boggs, D. H., Park, R. S. & Kuchynka, P. The planetary and lunar ephemerides DE430 and DE431. *IPN Progr. Rep.* **42**, 196 (2014).
38. Jacobson, R. A. & Lainey, V. Martian satellite orbits and ephemerides. *Planet. Space Sci.* **102**, 35–44 (2014).
39. Dehant, V., Defraigne, P. & Van Hoolst, T. Computation of Mars' transfer functions for nutations, tides and surface loading. *Phys. Earth Planet. Inter.* **117**, 385–395 (2000).
40. Van Hoolst, T., Dehant, V., Roosbeek, F. & Lognonné, P. Tidally induced surface displacements, external potential variations, and gravity variations on Mars. *Icarus* **161**, 281–296 (2003).
41. Archinal, B. A. et al. Report of the IAU Working Group on Cartographic Coordinates and Rotational Elements: 2015. *Celest. Mech. Dyn. Astron.* **130**, 22 (2018).
42. Konopliv, A. S., Yoder, C. F., Standish, E. M., Yuan, D.-N. & Sjogren, W. L. A global solution for the Mars static and seasonal gravity, Mars orientation, Phobos and Deimos masses, and Mars ephemeris. *Icarus* **182**, 23–50 (2006).
43. Dehant, V. et al. The radioscience LaRa instrument onboard ExoMars 2020 to investigate the rotation and interior of Mars. *Planet. Space Sci.* **180**, 104776 (2020).
44. Kahan, D. S. et al. Mars precession rate determined from radiometric tracking of the InSight lander. *Planet. Space Sci.* **199**, 105208 (2021).
45. Baland, R.-M., Hees, A., Yseboodt, M., Bourgoin, A. & Le Maistre, S. Relativistic contributions to the rotation of Mars. *Astron. Astrophys.* **670**, A29 (2023).
46. Lange, L. et al. InSight pressure data recalibration, and its application to the study of long-term pressure changes on Mars. *J. Geophys. Res. Planets* **127**, e2022JE007190 (2022).
47. de la Torre Juarez, M., Piqueux, S., Kass, D. M., Newman, C. & Guzewich, S. D. Pressure deficit in Gale crater and a larger northern polar cap after the Mars year 34 global dust storm. *AGU Fall Meeting Abstr*. P51C-02 (2019).
48. Kuchynka, P. et al. New constraints on Mars rotation determined from radiometric tracking of the Opportunity Mars Exploration Rover. *Icarus* **229**, 340–347 (2014).
49. Panning, M. P. et al. Planned products of the Mars structure service for the InSight mission to Mars. *Space Sci. Rev.* **211**, 611–650 (2017).
50. Connolly, J. A. D. Computation of phase equilibria by linear programming: a tool for geodynamic modeling and its application to subduction zone decarbonation. *Earth Planet. Sci. Lett.* **236**, 524–541 (2005).
51. Stixrude, L. & Lithgow-Bertelloni, C. Thermodynamics of mantle minerals – I. Physical properties. *Geophys. J. Int.* **162**, 610–632 (2005).
52. Greenwood, S., Davies, C. J. & Pommier, A. Influence of thermal stratification on the structure and evolution of the Martian core. *Geophys. Res. Lett.* **48**, e2021GL095198 (2021).
53. Terasaki, H. et al. Pressure and composition effects on sound velocity and density of core-forming liquids: implication to core compositions of terrestrial planets. *J. Geophys. Res. Planets* **124**, 2272–2293 (2019).
54. Tsuno, K., Grewal, D. S. & Dasgupta, R. Core–mantle fractionation of carbon in Earth and Mars: the effects of sulfur. *Geochim. Cosmochim. Acta* **238**, 477–495 (2018).
55. Okuchi, T. Hydrogen partitioning into molten iron at high pressure: implications for Earth's core. *Science* **278**, 1781–1784 (1997).
56. Clesi, V. et al. Low hydrogen contents in the cores of terrestrial planets. *Sci. Adv.* **4**, e1701876 (2018).
57. Malavergne, V. et al. Experimental constraints on the fate of H and C during planetary core–mantle differentiation. Implications for the Earth. *Icarus* **321**, 473–485 (2019).

58. Yuan, L. & Steinle-Neumann, G. Strong sequestration of hydrogen into the Earth's core during planetary differentiation. *Geophys. Res. Lett.* **47**, e2020GL088303 (2020).
59. Anderson, D. L. & Minster, J. B. The frequency dependence of Q in the Earth and implications for mantle rheology and Chandler wobble. *Geophys. J. R. Astron. Soc.* **58**, 431–440 (1979).
60. Yseboodt, M., Dehant, V. & Péters, M.-J. Signatures of the Martian rotation parameters in the Doppler and range observables. *Planet. Space Sci.* **144**, 74–88 (2017).

Acknowledgements This is InSight Contribution Number 211. The research done at the Royal Observatory of Belgium was supported by the Belgian PRODEX programme managed by the European Space Agency in collaboration with the Belgian Federal Science Policy Office, contract numbers PEA4000129361 and PEA4000140326. A.C. was supported by the French Community of Belgium within the frame of a FRIA grant. The work performed at the Jet Propulsion Laboratory, California Institute of Technology, was under contract with NASA. J.-C.M., D.A., J.B., M.D., H.S., M.W., P.L. acknowledge support from CNES and ANR (ANR-19-CE31-0008-08), and J.B., H.S. and P.L. thank IdEx Université de Paris (ANR-18-IDEX-0001). D.A. received funding from the European Research Council under the European Union's Horizon 2020 research and innovation programme (grant agreement 724690). Those authors computing BSL models were given access to the HPC resources of IDRIS under the allocation A011041317 made by GENCI. J.B. acknowledges support from the European Research Council under the European Union's Horizon 2020 research and innovation programme (grant agreement 101019965—ERC advanced grant SEPtiM).

Author contributions Writing the original draft: S.L.M., A.R., M.B., A.C., M.Y., R.-M.B., T.V.H., M.D. and H.S. Writing, review and editing: M.W. and D.A. Formal analysis: S.L.M. and A.C. Validation: D.B., A.K. and M.-J.P. Software: J.-C.M., S.L.M. and A.C. Data curation: D.K., D.B., S.L.M. and A.C. Methodology: A.R., M.Y., R.-M.B., M.B., T.V.H., D.A., J.B., M.D., A.-C.P., H.S. and N.T. Investigation: S.L.M., A.R., W.M.F., D.K. and D.B. Conceptualization: W.M.F., V.D. and P.L. Project administration: W.B.B., S.S. and M.P.

Competing interests The authors declare no competing interests.

Additional information

Supplementary information The online version contains supplementary material available at https://doi.org/10.1038/s41586-023-06150-0.

Correspondence and requests for materials should be addressed to Sébastien Le Maistre.

Peer review information *Nature* thanks Michael Efroimsky and the other, anonymous, reviewer(s) for their contribution to the peer review of this work.

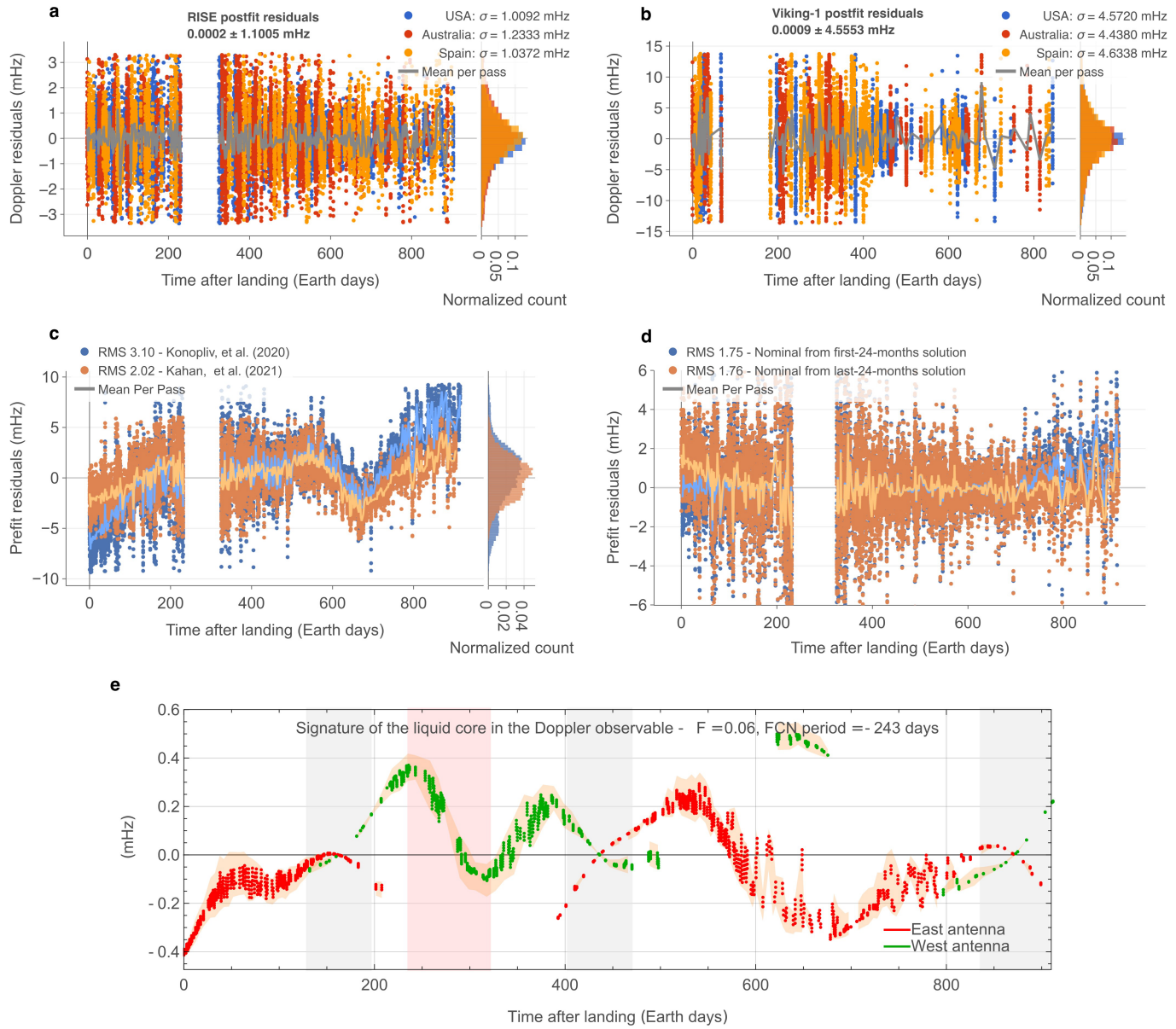

Extended Data Fig. 1 | RISE Doppler residuals and signature of the liquid core. Post-fit Doppler residuals and their histogram distributions for RISE **(a)** and Viking 1 lander **(b)** as a function of the mission time after landing and of the DSN facilities location. **(c)** Pre-fit Doppler residuals of RISE data as a function of time computed with the latest rotation models of Konopliv et al. (2020)[10] (in blue) and Kahan et al. (2021)[44] (in orange). **(d)** Pre-fit residuals with nominal values of the classical rotation model parameters coming from converged RISE solution using only the first 24 months of data (blue) and only the last 24 months of data (orange). This shows that the classical model fails at matching RISE full arc data since a clear trend is observed in the regions not covered by the corresponding nominal solution. **(e)** Theoretical signature of the liquid core for the RISE timing, separated in red for the East antenna and in green for the West antenna tracking. The FCN parameters are $F = 0.06$ and FCN period of −243 days. The orange envelope shows the signature when the FCN period is slightly different (between −238 and −248 days). The pink box is the interval where the SEP angle is smaller than 15° (conjunction) while the grey boxes are the intervals where the Earth declination is close to 0°. The signature of a parameter in the Doppler observable is the difference between the observable computed using a nominal/non-zero value for this parameter and that obtained when the parameter is set to 0[60].

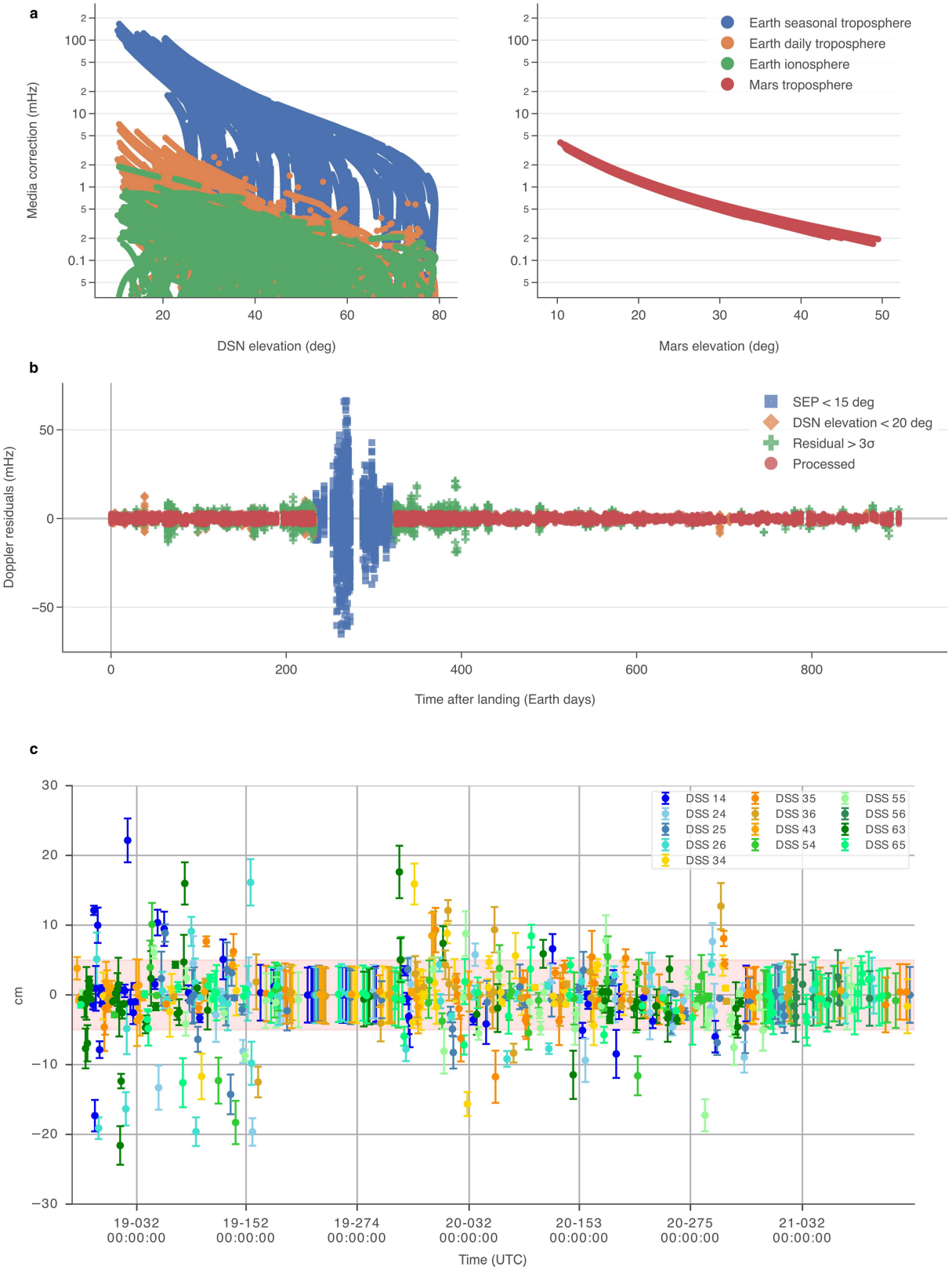

Extended Data Fig. 2 | RISE data calibrations. (a) Correction for media delays as applied to the RISE data points. On the left, the corrections due to the Earth's atmosphere as a function of the elevation at the DSN, on the right those due to Mars' troposphere, as a function of their elevation at Mars. **(b)** RISE Doppler residuals: only the red points are processed, i.e. used in our analysis. Points acquired at low elevation above the DSN station (orange diamonds) are affected by large noise from the Earth's atmosphere. They are still part of our analysis thanks to our accurate Earth noise calibration. The rest of the points are eliminated due to low SEP (blue squares), or high residual value (green crosses). **(c)** Estimated wet troposphere bias parameter per pass, classified by DSN station identifier. Shaded area is the a priori uncertainty.

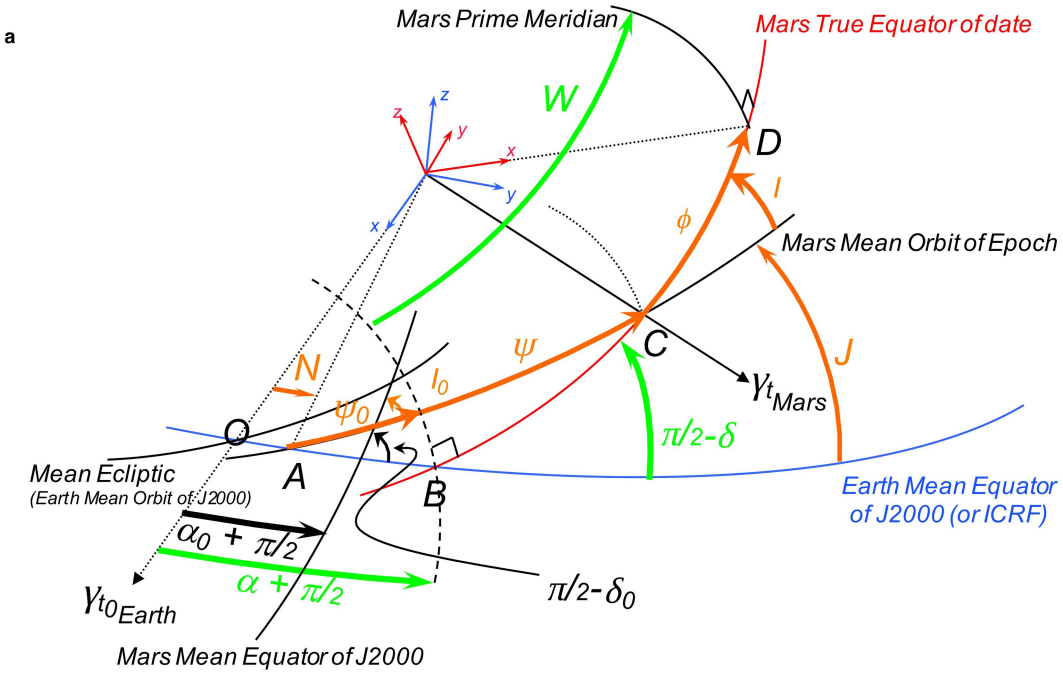

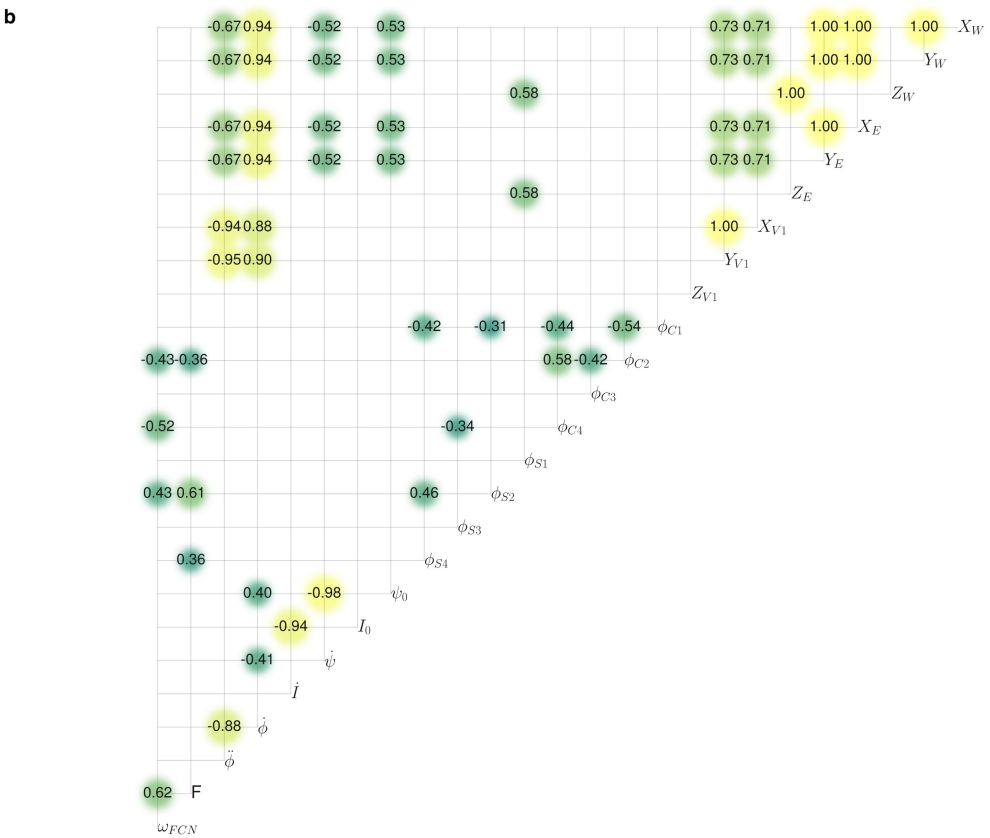

Extended Data Fig. 3 | Mars rotation and orientation angles and their correlations. (a) Reference frames and Mars orientation angles (orange and green) for conversion between the Earth mean equator of J2000 (in blue) and Mars body-fixed coordinates (in red). **(b)** Correlation matrix between MONTE solved parameters (GINS correlation matrix is equivalent) using the full set of RISE data (see Supplementary Table S1 for symbol definition). Values smaller than 0.3 are set to 0 for readability.

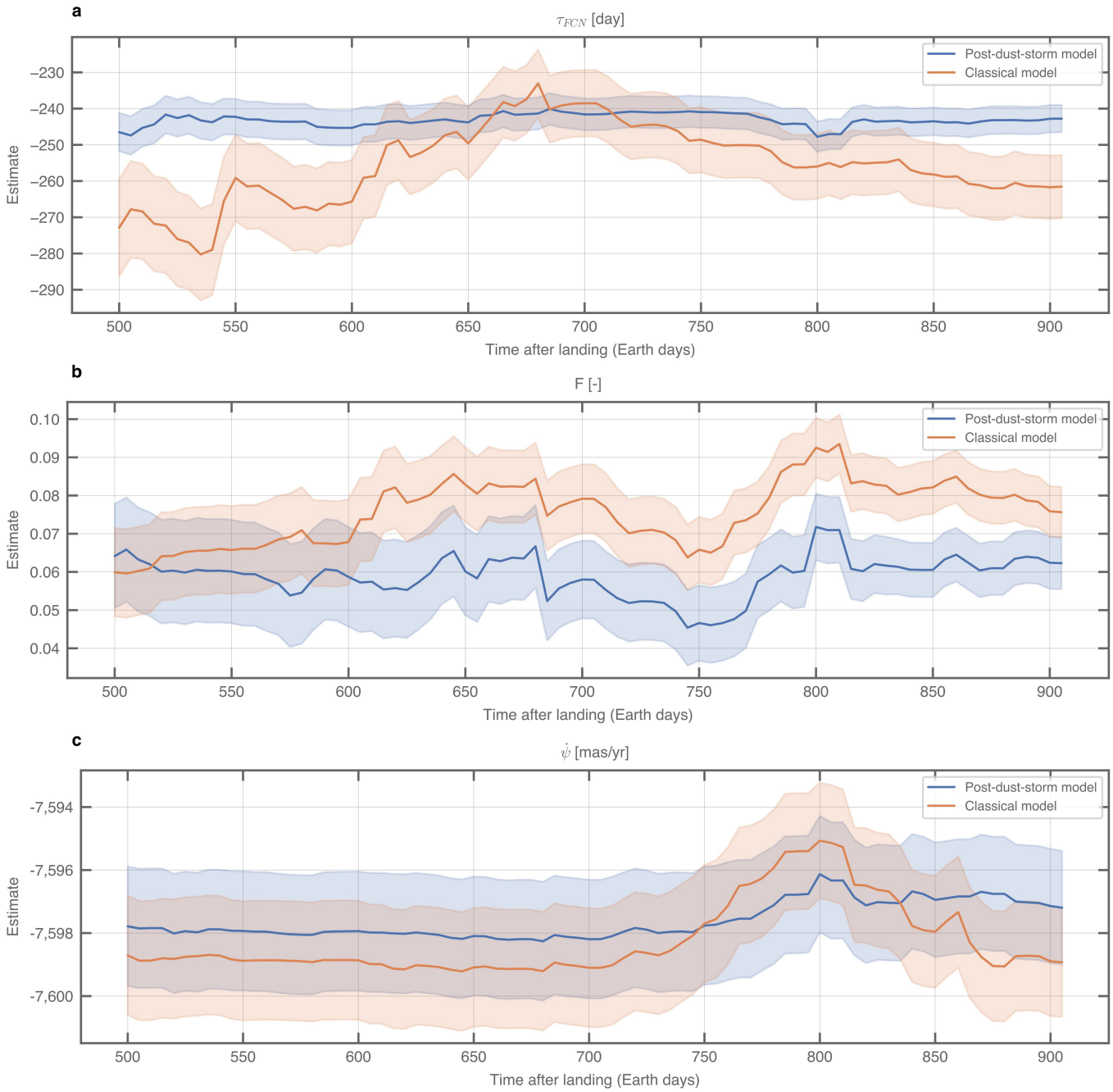

Extended Data Fig. 4 | Comparison between the classical model of rotation of Mars and the one proposed in this study. Temporal evolution of the 30-months solutions for the FCN period **(a)**, the core amplification factor **(b)**, and the precession rate **(c)**, with the classical spin model (orange) and with the model with corrections on the rotation rate for the post-dust-storm period (blue). Shaded envelopes are 1σ uncertainty bounds.

Extended Data Table 1 | 2-way Doppler data at 60 s of integration time considered in this study

Mission	Begin time dd-mm-yyyy	End time dd-mm-yyyy	Time span (days)	total/used nbr of 2-way Doppler	total/used tracking passes	Elevation at Mars (°)	Noise (mHz)
Viking 1	21-07-1976	30-12-1978	892	13,833/10,927	208/172	12-88	4.5
InSight	27-11-2018	31-05-2021	915	25,093/17,180	544/397	10-49	1.1

Extended Data Table 2 | Best solution of the main Mars rotation parameter estimates corresponding to an average of the GINS and MONTE sets of full arc solutions reported in Supplementary Table S1

Parameter	Symbol	Unit	Value and Uncertainty (Full arc)
Prime meridian at J2000	ϕ_0	deg	133. 3863940 ± 0.0000074
Longitude of node at J2000	ψ_0	deg	81.96835901 ± 0.000013
Precession rate	$\dot{\psi}$	mas/yr	-7,598.1 ± 2.2
Obliquity at J2000	I_0	deg	25.18940927 ± 0.0000064
Obliquity rate	$\dot{I}$	mas/yr	-7.99 ± 1.3
Rotation rate	$\dot{\phi}$	deg/day	350.891985339082 ± 0.000000011
Quadratic Rotation coefficient	$\ddot{\phi}$	deg/day^2	4.11 10^{-12} ± 9.1 10^{-13}
Core amplification factor	F	-	0.0615 ± 0.007
FCN period	τ_{FCN}	day	-243 ± 3.3
Spin variation amplitudes at InSight era	ϕ_{C1}	mas	400.0 ± 4.0
	ϕ_{C2}	mas	-109.1 ± 4.2
	ϕ_{C3}	mas	-9.7 ± 1.6
	ϕ_{C4}	mas	0.4 ± 2.1
	ϕ_{S1}	mas	-176.5 ± 1.7
	ϕ_{S2}	mas	-134.4 ± 3.1
	ϕ_{S3}	mas	-22.2 ± 2.3
	ϕ_{S4}	mas	-11.7 ± 0.8

Uncertainties are $\sigma = \sqrt{((\sigma_M^2 + \sigma_G^2 + (p_M - p_G)^2)/2)}$, where $p_M \pm \sigma_M$ and $p_G \pm \sigma_G$ are MONTE and GINS solutions (central value plus or minus formal errors), respectively.